PCCP

ROYAL SOCIETY OF CHEMISTRY

PAPER

View Article Online
View Journal | View Issue

Cite this: *Phys. Chem. Chem. Phys.*, 2025, **27**, 18162

Molecular mobility and electrical conductivity of amino acid-based (DOPA) ionic liquid crystals in the bulk state and nanoconfinement

Mohamed A. Kolmangadi,†[a] Aileen R. Raab,[b] Paulina Szymoniak,[a] Zhuoqing Li,[c] Patrick Huber,[cd] Sabine Laschat[b] and Andreas Schönhals*[ae]

This study explores the molecular mobility, phase behavior, and electrical conductivity of dihydroxyphenylalanine-based ionic liquid crystals (DOPA*n*, with alkyl side chains *n* = 12, 14, 16) featuring cyclic guanidiniumchloride headgroups, in both bulk and nanoconfined states. Using broadband dielectric spectroscopy, differential scanning calorimetry, and fast scanning calorimetry, the research uncovers a complex interplay between molecular structure, self-assembly, and molecular mobility. In bulk, DOPA*n* shows a phase sequence from plastic crystalline to hexagonal columnar and isotropic phases, driven by superdisc formation and columnar organization. Multiple relaxation processes are identified: localized side-chain dynamics (γ-relaxation), ionic headgroup or core motions (α_1-relaxation), and cooperative alkyl domain fluctuations (α_2-relaxation). Conductivity decreases with increasing side chain length. Under nanoconfinement in anodic aluminum oxide membranes, phase behavior changes: the Col_h–Iso transition is suppressed, and a new α_3-relaxation appears, linked to dynamics in an adsorbed interfacial layer. DC conductivity drops by up to four orders of magnitude due to confinement effects, altered molecular orientation, and phase transitions—especially the emergence of a nematic-like state in DOPA16. These findings highlight the importance of molecular design, pore geometry, and surface chemistry in tuning ionic liquid crystal properties for advanced applications in nanofluidics, ion transport, and responsive materials.

Received 24th June 2025,
Accepted 14th August 2025

DOI: 10.1039/d5cp02406d

rsc.li/pccp

Introduction

Ionic liquid crystals (ILCs) are an innovative class of ionic liquids that demonstrate mesomorphic behavior within a specific temperature range, specifically above their melting point and below their clearing point. These materials exhibit the ordered molecular structure characteristic of liquid crystals due to self-assembly, combined with anisotropic physical properties and ionic conductivity like that of ionic liquids. ILCs can be considered as salts built from large organic cation and anions.[1–6] Ionic liquid crystals are promising candidates for optoelectronic and biological applications due to their inherent properties. They are frequently water-soluble, capable of aligning on various substrates, and can be processed using multiple cost-effective techniques.[7] The range of applications of ILCs also covers electrolytes for batteries,[8] supercapacitors,[9] micro-fluidic devices as well as in dye-sensitized solar cells.[10] Besides these applications also the biological activity of ionic liquid crystals has been studied in some detail.[11–15] This includes also the effects of ILCs on enzymatic reactions.[16]

Columnar ionic liquid crystals are a specific type of ILCs that exhibit a columnar mesophase. In this phase, the molecules of the ILCs self-assemble into one-dimensional columns, primarily driven by π–π interactions between the aromatic cores, which are surrounded by mobile alkyl side chains. These columns can further self-organize into distinct lattice structures, which may be hexagonal, rectangular, oblique, or rectangular in nature.[17] The hexagonal columnar phase (Col_h) is the most frequently observed mesophase of discotic ionic liquid crystals, characterized by the organization of columns into a planar hexagonal arrangement, conforming to a two-dimensional *P6mm* lattice structure.[18]

Columnar ionic liquid crystals are capable of transporting water[19] and ions,[20] and can also be utilized as bioactive

[a] *Bundesantalt für Materialforschung und-prüfung (BAM), Unter den Eichen 87, 12205 Berlin, Germany. E-mail: Andreas.Schoenhals@bam.de; Fax: +49 30/8104-73384; Tel: +49 30/8104-3384*
[b] *Institut für Organische Chemie, Universität Stuttgart, Pfaffenwaldring 55, 70569 Stuttgart, Germany*
[c] *Institute for Materials and X-ray Physics, Hamburg University of Technology, Denickestraße 15, 21073 Hamburg, Germany*
[d] *Centre for X-ray and Nano Science CXNS, Deutsches Elektronen-Synchrotron DESY, 22607 Hamburg, Germany*
[e] *Institut für Chemie, Technische Universität Berlin, Straße des 17. Juni 135, 10623 Berlin, Germany*
† Physics & Material Science EMEA, Covestro Deutschland AG, 51373 Leverkusen, Germany.

compounds as discussed above.[11–16] Understanding the structure–property relationships, including molecular mobility, charge transport, and phase behavior, is essential as these factors directly influence the properties of the columns.

Guanidinium-based ionic liquid crystals exhibit high ionic conductivity and tunable mesophases due to their cyclic guanidinium headgroup, which enables strong electrostatic and hydrogen-bonding interactions. Combined with aromatic cores and flexible alkyl chains that promote π–π stacking and dynamic self-assembly. This molecular architecture imparts versatile ion transport properties and phase behaviors. Investigations on guanidinium-based columnar ionic liquid crystals in the bulk state encompass examining the effects of the cation headgroup and the alkyl chain length on the stability of the mesophase, as well as their impact on charge transport properties.[21–23] Minor modifications in the molecular structure influence the macroscopic properties of the system. ILCs with a cyclic cation headgroup exhibit higher direct current (DC) conductivity and enhanced molecular mobility compared to their acyclic counterparts.[22] Additionally, a systematic variation in the alkyl chain length of ILCs has shown that those with alkyl side chains length of 8 and 10 carbon atoms exhibited a behavior which is more comparable to ionic liquids, characterized by a narrow mesophase window. In contrast, ILCs with longer alkyl side chains lengths (n = 12, 14, 16) display a broader mesophase range but a reduced electrical conductivity as supported by coarsed-grained molecular dynamic simulations.[24]

Ionic liquids (Il) have been also confined to nanopores. The aim of confining ILs is for instance to achieve an orientation of the columnar structure for ion or water transport. The nanoconfinement of ionic liquids can result in either an enhancement or reduction of the ionic conductivity relative to their bulk state depending on factors such as pore size, alkyl chain length *etc.* Tu *et al.*[25] investigated the confinement of pyrrolidinium-based ionic liquids with side chain lengths of 6 and 10 carbon atoms in porous anodic aluminum oxide with pore sizes of 80 nm and 10 nm. They found an increase in the electrical conductivity for the IL with the shorter side chain length, whereas a 300-fold reduction in the ionic conductivity was noted for the IL with the longer side chain. The distinct conduction behaviors of nonconfined long and short chain ionic liquids (ILs) remain unresolved. In the case of conventional liquid crystals (LCs) confined within porous anodic aluminum oxide, several common characteristics have been observed: (i) the molecular dynamics typically decelerate compared to the bulk state, and (ii) there is a reduction in the transition temperatures, with decreasing pore size often adhering to the Gibbs–Thomson relation.[26,27]

A recent study investigated the molecular mobility and phase transition behavior of guanidinium-based columnar ILCs confined within the nanopores of self-ordered anodic aluminum oxide membranes with varying pore diameters (25–180 nm). The study employs broadband dielectric spectroscopy (BDS), calorimetry, and X-ray scattering to elucidate how pore size and pore surface chemistry (hydrophobic or hydrophilic) influence the molecular dynamics and phase transition behavior of this system.[28] Differential scanning calorimetry (DSC) investigations reveal in the heating run that firstly the phase transition temperature from the plastic crystalline to the liquid crystalline state exhibits a nonmonotonic dependence on the inverse pore diameter, and secondly that the transition from the liquid crystalline to the isotropic phase is suppressed for all nanoconfined samples. This suppression, observed in the thermal signal, is corroborated by BDS and X-ray scattering. It is proposed that this transition occurs as a continuous phase transition within the pores, rather than as a discontinuous first-order transition observed in the bulk state. BDS investigations indicate distinct relaxation processes for the bulk and nanoconfined ILCs which are assigned in detail. Additionally, it is demonstrated that the self-assembly of this ILC is dynamic, a characteristic that may extend to other ILCs as well.

In this study the molecular mobility of a homologous series of amino acid based ILCs DOPAn is studied by broadband dielectric spectroscopy and advanced calorimetry. The length of the aliphatic side chains characterized by the number of its carbon atoms n is systematically varied from 12 over 14 to 16. In addition, the considered ILCs are nanoconfined to ordered anodic aluminum oxide membranes with different pore diameters. Recently the same system was investigated by high resolution optical birefringence measurements and 3D reciprocal space mapping based on synchrotron X-ray scattering to reveal orientation and phase transition of the ILCs in a nanometric confinement.[29]

Materials and methods

Materials and sample preparation

The synthesis of the 3,4-dihydroxyphenylalanine based ionic liquid crystal is described in detail in ref. 15. The building molecule is based on L-3,4-dihydroxydroxyphenylalanine (L-DOPA). Its chemical structure is given in Fig. 1. The DOPAn molecules consists of a large cyclic organic guanidinium cation, hydrophilic aromatic core and three hydrophobic alkyl side chains. The counter anion is chloride. The number of carbon atoms n in the alkyl side chains is n = 12,14,16. The shape of a single DOPA molecule is conical, related to the presence of the three alkyl side chains.

Upon heating, the DOPAn compounds with an acrylic organic guanidinium cation show three different phases. At low temperatures several plastic crystalline phases (Cry) are observed followed by a hexagonal columnar liquid crystalline phase (Col_h) and the isotropic state (Iso) at the highest temperature. This phase sequence was confirmed by X-ray scattering as well as polarized

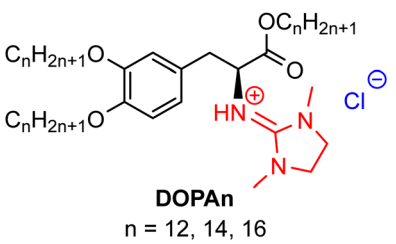

Fig. 1 Chemical structure of building molecules based on L-3,4 dihydroxyphen-ylalanine consisting of an aromatic core with a guanidinium headgroup (red) and alkyl side chains. The chloride counter ion is indicated in blue.

optical microscopy.[15] The phase behavior of the DOPA*n* materials with the cyclic guanidinium cation is discussed below.

Disk-like molecules are responsible for the formation of a columnar mesophase in conventional discotic liquid crystals (see for instance ref. 30 and 31). In the considered case, the DOPA*n* building molecules are wedge-shaped. Nevertheless, a columnar phase is observed (see below). This is due to a twofold self-assembling process. In a first step, six DOPA*n* molecules form a disk-like structure due to ionic interactions (see Fig. 2). This disc-like structure is called "superdisc" in the following. In the second self-assembling step the superdiscs form one-dimensional columns which are arranged on a hexagonal lattice. The intercolumnar space is filled with the flexible alkyl side chains which leads to a nanophase separated structure consisting of columns and alkyl chains in the intercolumnar space.

Anodic aluminum oxide (AAO) disk-shaped membranes were purchased from Smart Membranes GmbH (Halle, Germany). The membranes had a diameter of 15 mm and a thickness of 80 μm. The pore diameter was 180 nm with a porosity of 14.5%, 80 nm with a porosity of 37% and 25 nm with a porosity of 10%. This data was provided by the producer. Before the infiltration of the DOPA*n* molecules into the pores of the membranes, they were first degassed under vacuum (10^{-4} mbar) at 473 K for 5 h in order to remove physical bounded impurities or adsorbed water (as much as possible). After this cleaning step the membranes were transferred under vacuum to a glove box filled with argon. The quantity of material necessary to fully occupy the pores was calculated based on the pore volume and membrane porosity, assuming a density of 1 g cm^{-3}. A slight excess to the calculated amount of the ionic liquid crystal was applied to the membranes and infiltrated at 20 K above the clearing point for 48 h under argon atmosphere. The typical masses within the membranes were a few milligrams. Before conducting the measurements, the excess ILC was meticulously removed from the surface of the anodic aluminum oxide (AAO) membranes using a sharp knife. Due to the less availability of the different DOPA*n* materials not all systems could be confined to all pore sizes. An overview of the conducted experiments is given in Table 1.

Anodic aluminum oxide (AAO) membranes exhibit inherent hydrophilicity. To examine the impact of pore wettability, the surface of the pore walls was chemically modified to render them hydrophobic. This modification was achieved using *n*-octadecylphosphonic acid (ODPA), following the methodology outlined in ref. 32. ODPA, sourced from Alfa Aesar, was utilized without further purification. The modification procedure is summarized in detail elsewhere.[33]

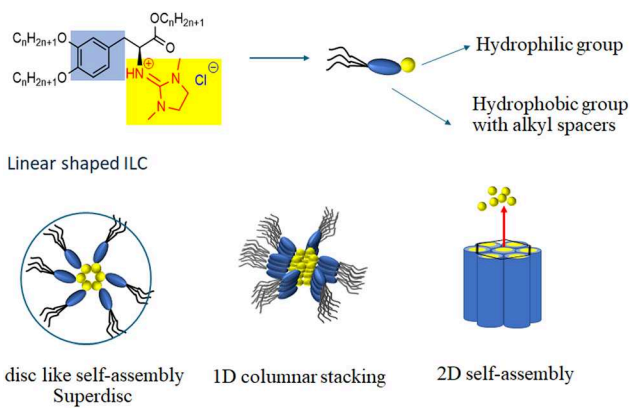

Fig. 2 Self-assembly of the DOPA*n* ILCs.

Table 1 Conducted experiments for the confined samples

	DOPA12		DOPA14		DOPA16	
Pores size	BDS	DSC	BDS	DSC	BDS	DSC
180 nm	X	—	X	—	X	X
80 nm	—	—	—	—	—	X
25 nm	X	—	X	—	X	—

Differential scanning calorimetry (DSC)

The thermal properties of both bulk and confined ionic liquid crystals were analyzed using a PerkinElmer DSC 8500 differential scanning calorimeter. Approximately 6 mg of the sample was placed in a standard aluminum pan. Measurements were conducted over a temperature range of 203 K to 463 K, with heating and cooling rates set at 5 K min^{-1}. Nitrogen was used as the purge gas at a flow rate of 20 ml min^{-1}. The thermal scans followed a sequence of heating, cooling, heating, cooling, and a final heating step. The measured thermal events are reproducible in the consecutive thermal cycles. The heat flow measured for the samples was corrected for the baseline. The baseline was obtained by fitting a polynomial of third order to the data by excluding the phase transitions. This base line was subtracted from the measured data for the DOPA*n* samples. Prior to all measurements, the instrument was calibrated using Indium as a standard. The second heating run was used for analysis.

For the DSC measurements of the confined samples the filled membrane was broken into small pieces. The pieces then were carefully packed in the DSC pan to ensure a good thermal contact.

Fast scanning calorimetry (FSC)

To investigate a possible thermal glass transition in the samples fast scanning calorimetry (FSC) was employed using a Flash DSC 1 (Mettler Toledo, Columbus, USA). The Flash DSC 1 is an adiabatic power compensated DSC.[34] By chip-based technology it allows for heating rates between 10 K s^{-1} and 10^4 K s^{-1}. The cooling rates are approximately one order of magnitude lower. The sample cells were MultiSTAR UFS1 twin chip sensors. The samples masses were in the range of several 100 ng. The base temperature of the chip was controlled by a Huber TC100 intracooler. The calorimeter chip was purged by nitrogen with a rate of 40 ml min^{-1}. Prior to the measurement, the sensor was conditioned, and the signal was corrected as advised by the manufacturer.

To ensure a good thermal contact of the samples with the measuring cell the DOPA*n* materials were melted on the calorimeter chip at temperatures above the clearing temperature. Measurements were carried out at different heating rates.

To have the same thermal history of the sample, it was cooled down with the rate of 1000 K s^{-1} before each heating run employing different heating rates.

Broadband dielectric spectroscopy (BDS)

Dielectric spectroscopic investigations were conducted using a high-resolution ALPHA analyzer (Novocontrol, Montabaur, Germany), interfaced to a sample holder equipped with an active sample head. The sample temperature was precisely controlled by a Quatro temperature controller (Novocontrol), maintaining a stability within 0.1 K. All dielectric measurements were performed in a parallel plate geometry.

For the bulk ionic liquid crystals (ILCs), the sample was placed between gold-plated brass electrodes with a diameter of 10 mm, separated by 50 μm, using fused silica spacers. For ILCs confined in anodic aluminum oxide (AAO), the disk-like membrane was positioned between two gold-plated electrodes, also 10 mm in diameter, with an 80 μm spacing provided by the membrane thickness. The confined ILC in AAO can be modeled as two parallel plate capacitors, consisting of ILC in the pores and AAO membrane, with the total permittivity related to the individual values through the complex dielectric function $\varepsilon^*(f) = \varepsilon'(f) - i\varepsilon''(f)$ where ε' and ε'' are the real and imaginary parts of the complex dielectric function, f denotes frequency, and $i = \sqrt{-1}$ is the imaginary unit. Isothermal frequency scans were performed over a range from 10^{-1} Hz to 10^6 Hz, covering temperatures from 133 K to 365 K. The measurements followed a sequence of heating, cooling, and heating. It is noted that the dielectric loss is not scaled by the porosity, and since only the relaxation rate is discussed quantitatively, this procedure does not introduce errors. For the conductivity the data are scaled by the porosity as absolute values are considered.

Results and discussion

Bulk samples

Phase behavior. Fig. 3 depicts the heat flow *versus* temperature for the different DOPA*n* materials. At low temperature the thermograms show at least one crystal–crystal transition and then a strong phase transition from plastic crystalline phase (Cry) to the columnar hexagonal ordered (Col_h, *P6mm*) one at higher temperatures. At even higher temperatures the phase transition from the Col_h phase to the isotropic state is observed. The assignment of the phases was further confirmed by experiments employing a polarizing optical microscopy (see Fig. S1) and X-ray scattering (see Fig. S2). Lattice parameters *etc.* are given in the Supporting information. It is worth noting that the phase transition enthalpies for the transition from the columnar hexagonal to isotropic state are much smaller than that of the transition from the plastic crystalline to the columnar hexagonal ordered state. This behavior is due to the formation of superdiscs from six linear molecules by electrostatic interactions which are relatively weak compared to chemical bonds.

Besides the phase transition there is evidence that in the plastic crystalline phase related materials also undergo a glass transition (see for instance ref. 21 and 28). Although no clear step in the in the heat flow indicating a glass transition is observed by conventional calorimetry it might be discussed whether the DOPA*n* materials also undergo a glass transition. This problem will be discussed in more detail below by employing fast scanning calorimetry in the molecular mobility section.

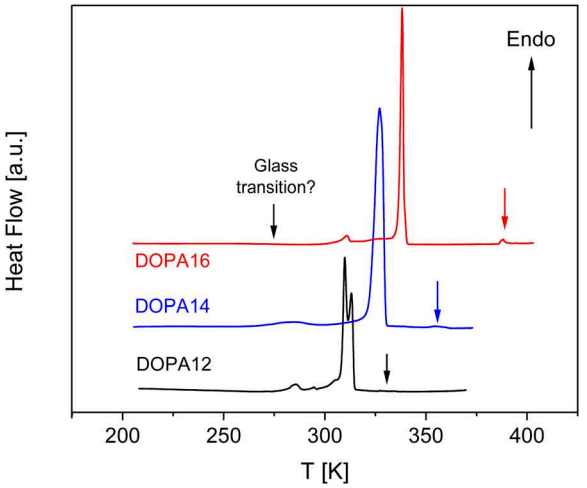

Fig. 3 Heat flow *versus* temperature for the considered ionic liquid crystals (second heating run, heating rate 5 K min^{-1}): black – DOPA12, blue – DOPA14, red – DOPA16. The curves are shifted along the *y*-scale for sake of clearness. The phase transition from the Col_h to the isotropic state is marked by down sited arrows.

Molecular mobility. The dielectric spectra for the DOPA*n* materials show different dielectric active processes in the bulk state (see Fig. 4). At low temperatures a γ-relaxation is observed. With increasing temperature, the γ-relaxation is followed by a so-called α_1-relaxation. The molecular assignment of these relaxation processes will be discussed in detail below. At even higher temperatures the dielectric loss increases strongly with

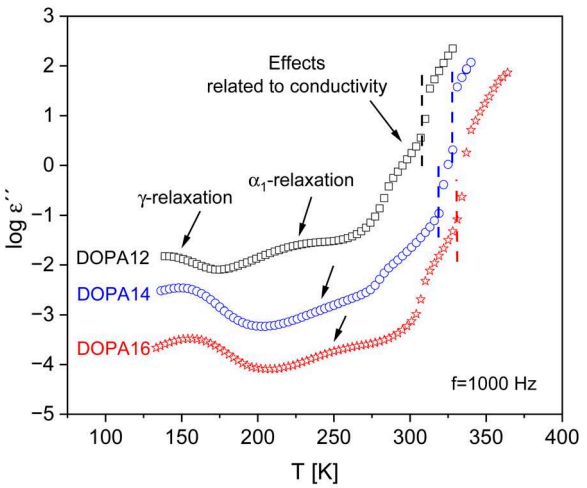

Fig. 4 Dielectric loss *versus* temperature at a frequency of 1000 Hz for the considered ionic liquid crystals: black – DOPA12, blue – DOPA14, red – DOP16. The dashed lines indicate the phase transition. The curves are shifted along the *y*-scale for sake of clearness: DOPA14 – −0.7; DOPA16 – −1.7.

temperature. This increase of dielectric loss is due to electrical conductivity and conductivity related effects. The latter effects can be due either to Maxwell/Wager/Sillars (MWS) and/or electrode polarization. The conductivity in the considered ILCs is due to the drift motion of ions. MWS and electrode polarization are related to the blocking of charge carriers at mesoscopic and macroscopic length scales, respectively. Employing a derivative approach to the dielectric permittivity, it could be shown for a related system in ref. 28, that a further relaxation process is hidden under these conductive related contributions to the dielectric loss.

The relaxation processes are analyzed by fitting the model function of Havrilak/Negami (HN) function to the data. The HN-function is given by[35]

$$\varepsilon^*_{\mathrm{HN}}(\omega) = \varepsilon_\infty + \frac{\Delta\varepsilon_{\mathrm{HN}}}{\left(1 + (\mathrm{i}\omega\tau_{\mathrm{HN}})^\beta\right)^\gamma}. \quad (1)$$

ω denotes the angular frequency $\omega = 2\pi f$. ε_∞ is the real part of the complex primitivity for $\varepsilon_\infty = \lim_{\omega \gg \tau_{\mathrm{HN}}^{-1}} \varepsilon'(\omega)$. The parameter $\Delta\varepsilon_{\mathrm{HN}}$ represents the dielectric strength. The relaxation time, τ_{HN}, corresponds to the frequency at which the dielectric loss reaches its maximum, denoted as f_{p} (relaxation rate). The relaxation rate f_{p} is calculated from the relaxation time by[36]

$$f_{\mathrm{p}} = \frac{1}{2\pi\tau_{\mathrm{HN}}}\left[\sin\frac{\beta\pi}{2+2\gamma}\right]^{1/\beta}\left[\sin\frac{\beta\gamma\pi}{2+2\gamma}\right]^{-1/\beta} \quad (2)$$

The parameters β and γ ($0 < \beta$; $\beta\gamma \leq 1$) characterize the symmetric and asymmetric broadening of the relaxation spectrum in comparison to the Debye model.[36] The conductivity is considered in the fitting process by adding $\frac{\sigma_0}{(\omega^s\varepsilon_0)}$ to the dielectric loss part of the HN-function. σ_0 is related to the DC conductivity but also includes contributions of Maxwell/Wagner/Sillars and/or electrode polarization. The parameter $s \leq 1$ characterizes non-ohmic effects in conductivity, where $s = 1$ indicates ohmic conductivity. The symbol ε_0 represents the permittivity of free space. For more details see ref. 36. Fig. 5(a) gives an example for the fit of the HN-function to the data of the γ-relaxation of DOPA16. From the relaxation rate f_{p} of the γ-relaxation is obtained and plotted *versus* inverse temperature in the relaxation map (see Fig. 6(a)). The temperature dependence of f_{p} is linear when plotted *versus* $1/T$ and can be described by the Arrhenius equation which reads

$$f_{\mathrm{p}} = f_\infty \exp\left(-\frac{E_{\mathrm{A}}}{RT}\right). \quad (3)$$

Here f_∞ is a pre-exponential factor and E_{A} the activation energy. R denotes the general gas constant.

For the activation energy the following values were estimated: DOPA12 – 25.9 kJ mol^{-1}; DOPA14 – 31.7 kJ mol^{-1}; DOPA16 – 33.5 kJ mol^{-1}. These numbers indicate that the γ-relaxation is due to a localized relaxation process. Moreover, the activation energy increases with increasing length of the alkyl side chain (see Fig. 6(b)). Both observations suggests that the γ-relaxation is related to localized fluctuation in the alkyl side chains. The dependence of E_{A} for the γ-relaxation of the DOPA series is different than that of the activation energy found for ILCs based on a phenylalkoxy benzoate aromatic core with a cyclic guanidinium cation headgroup (for the structure see inset of Fig. 6(b)) with a triflate as counterion, where a plateau is found for comparable side chain length although the absolute values are comparable.[23] The reason for the different behavior might be due to the different molecular core structures.

In Fig. 6(a) the temperature dependence of the relaxation rate of the γ-relaxation of polyethylene (PE) is included.[37] The γ-relaxation of PE takes place in a similar temperature and frequency range as the γ-relaxations of the DOPA*n* materials with a comparable activation energy. Therefore, it is concluded that the γ-relaxation of DOPA*n* is due to localized fluctuations in the alkyl side chain. Nevertheless, some polar components must be also involved. The inset of Fig. 6(a) gives log f_∞ *versus* the activation energy in the compensation plot (Meyer–Neldel) plot.[38–40] The data point for polyethylene matches the regression line of the DOPA*n* materials. There is some consensus in

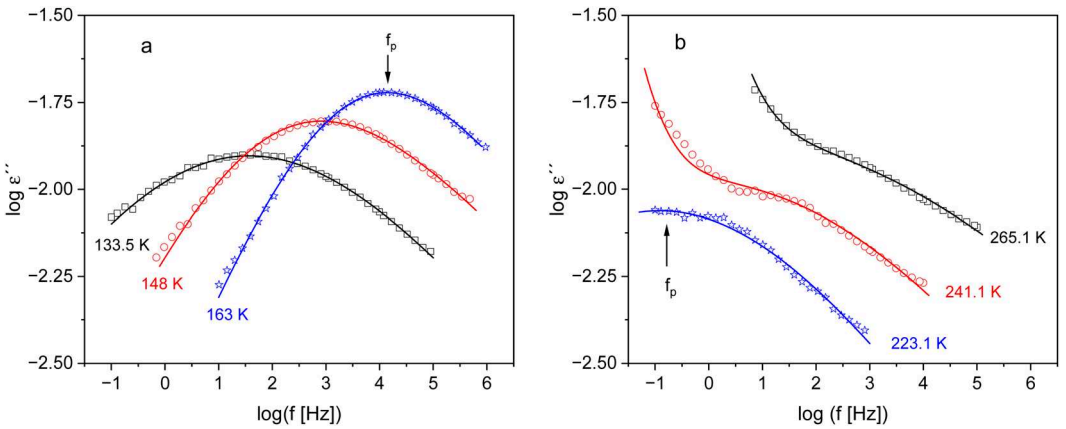

Fig. 5 (a) Dielectric loss *versus* frequency in the temperature region of the γ-relaxation of DOPA16: black squares – T = 133.5 K, red circles – T = 148 K, blue asterisk – T = 163 K. Lines are fits of the HN-function to the corresponding data. (b) Dielectric loss *versus* frequency in the temperature region of the α_1-relaxation of DOPA14: blue asterisk – T = 223.1 K, red circles – T = 241.1 K, black squares – T = 265.1 K. Lines are fits of the HN-function to the corresponding data.

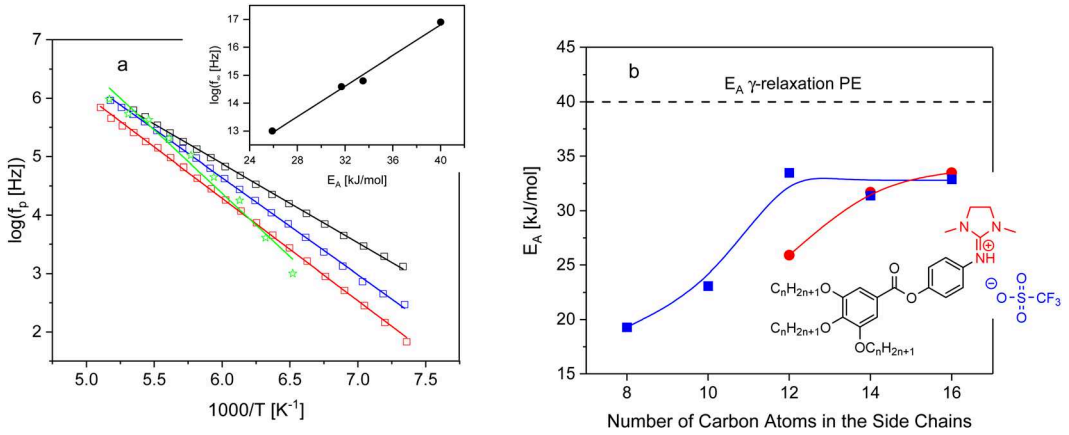

Fig. 6 (a) Relaxation rate of the γ-relaxation *versus* inverse temperature: black squares – DOPA12, blue squares – DOPA14, red squares – DOPA16, green asterisk – data for the γ-relaxation of polyethylene. The line are fits of the Arrhenius equation to the corresponding data. The inset gives $\log f_\infty$ *versus* the activation energy of the γ-relaxation in the compensation law. The line is a linear regression to the data. (b) Activation energy of the γ-relaxation *versus* the number of the carbon atoms in the alkyl side chain: red circles – DOPA*n*; blue squares – for the ILC with the structure given in the inset. The lines are guides to the eyes.

the literature suggesting that the molecular basis of the Meyer–Neldel law can be attributed to the cooperative behavior of the underlying molecular fluctuations.[38,39] Therefore, it might be concluded that some cooperative effects are involved in the γ-relaxation of DOPA*n*. The result that the activation energy of the γ-relaxation increases with increasing length of the side chain and that the Meyer–Neldel law is fulfilled including PE supports this interpretation. It is worth noting that a Meyer–Neldel compensation law was also found for localized relaxation processes for liquid crystalline side chain polymers.[41]

The HN-function is also fitted to the data of the α_1-relaxation. Examples for these fits are given in Fig. 5(b). The relaxation rates for the α_1-relaxation are depicted in the Arrhenius diagram (see Fig. 7) and is curved when plotted *versus* $1/T$ indicating a glassy dynamic related to a glass transition. The data can be described by the Vogel/Fulcher/Tammann (VFT-) equation which reads[42–44]

$$\log f_p = \log f_\infty - \frac{A}{T - T_0}. \quad (4)$$

A VFT-like temperature dependence of the relaxation rates indicates glassy dynamics related to a glass transition. The parameter f_∞ denotes the pre-exponential factor. Furthermore, A represents a fitting constant, while the temperature T_0 corresponds to the Vogel or ideal glass transition temperature. This temperature is typically located 30–70 K below the thermal glass transition temperature measured by DSC. The parameter A is related to the fragility, which is a quantity to characterize glass forming systems. A glass former is called strong when the temperature dependence of the relaxation rates is close to an Arrhenius behavior or fragile in the case when it follows the VFT-equation.[45]

The temperature dependence of the relaxation rates of the α_1-relaxation shifts slightly to higher temperatures with increasing length of the side chain. Moreover, it seems that the fragility increases from DOPA12 to DOPA14. However, it decreases then for

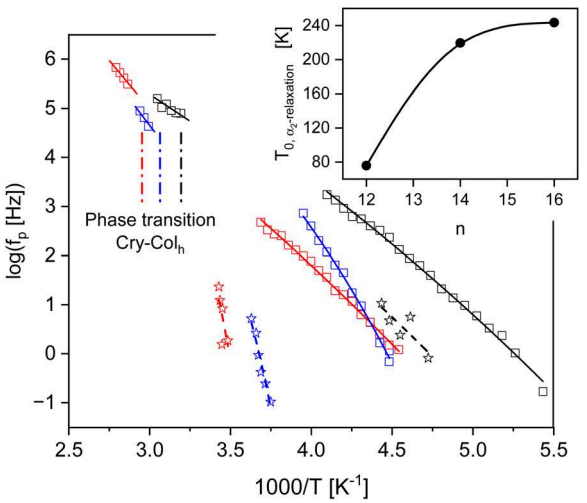

Fig. 7 Relaxation rates *versus* temperatures for the bulk DOPA*n* samples: squares – α_1-relaxation, asterisk – α_2-relaxation. Black – DOPA12, blue – DOPA14 and red – DOPA16. Solid lines – fits of the VFT equation to the corresponding data. The dotted dashed lines indicate the phase transition temperatures from the plastic crystalline to the hexagonal ordered liquid crystalline phase in the same color code. The inset gives the Vogel temperature of the α_2-relaxation *versus* the number of carbon atoms in the side chain.

DOPA16 in comparison to DOPA14. To understand this behavior further investigations on other ILCs with a comparable structure are necessary. The α_1-relaxation is also observed in the hexagonal columnar liquid crystalline phase. Due to the accessible frequency range, it can be traced only in a limited temperature range. For DOPA12 and DOPA16 the temperature dependence of the relaxation rates seems to agree with that in the plastic crystalline phase. This is not the case for DOPA14. The molecular assignment of the α_1-relaxation will be discussed below.

To investigate the glass transition behavior of the DOPA*n* ILCs further, fast scanning calorimetry was carried out. Fig. 8(a)

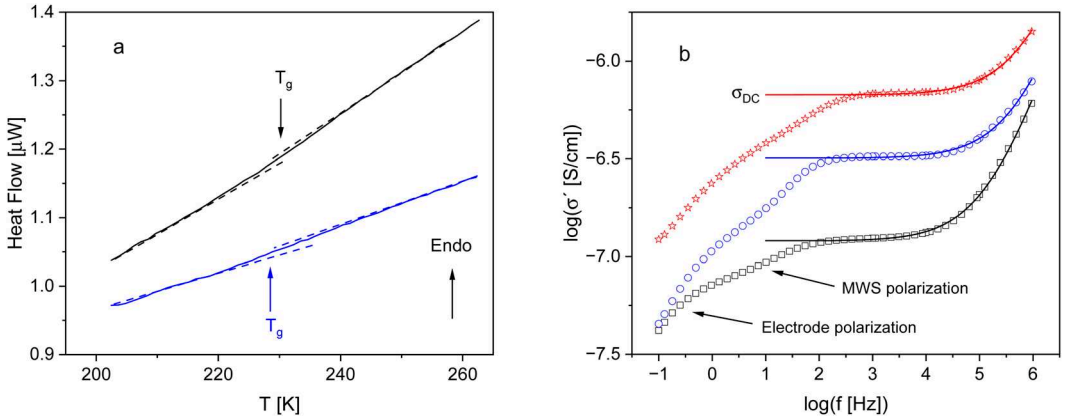

Fig. 8 (a) Heat flow *versus* temperature for DOPA12: blue – 500 K s^{-1} and black – 1000 K s^{-1}. The data for the heating rate of 500 K s^{-1} was shifted by 0.45 μW for sake of clearness. (b) Real part of the complex conductivity *versus* frequency: black squares DOPA12 at T = 328.1 K, blue circles – DOPA14 at T = 340 K and red asterisk – DOPA16 at T = 352.1 K. Lines are fits of eqn (7) to the corresponding data.

gives the heat flow *versus* temperature for DOPA12 for two different heating rates measured by FSC. The heat flow shows a step-like change which shifts to higher temperature with increasing heating rate. This behavior indicates a glass transition. The glass transition temperatures were determined by analyzing the midpoint of the step-like change in heat flow. In the framework of the fluctuation approach to the glass transition[46] a thermal relaxation rate can be estimated from the heat flow by

$$f_p = \frac{\dot{T}}{2\pi a \Delta T_g} \quad (5)$$

Here the heating rate is denoted by $\dot{T}$, and the width of the glass transition region is represented by ΔT_g. The value of ΔT_g was calculated as the difference between the endset and onset temperatures of the step-like change in the heat flow of the glass transition. The constant a has an approximate value of one. The underlying glassy dynamics is called α_2-relaxation.

The obtained thermal relaxation data are plotted against the inverse temperature in the Arrhenius plot (Fig. 7). The temperature dependence of the α_2-relaxation shifts to higher temperature with increasing length of the side chain. It follows also the VFT equation. The estimated Vogel temperature of the α_2-relaxation is plotted *versus* the number of carbon atoms in the inset of Fig. 7. T_0 increases strongly if n increases from 12 to 14 and then T_0 seems to reach a plateau for n = 16.

The temperature positions of the α_2-relaxation do not coincide with that of the α_1-relaxation. Moreover, the α_2-relaxation is not observed in the dielectric spectra. Therefore, it is concluded that the underlying molecular mechanisms of the α_1- and α_2-relaxation are different. As the α_2-relaxation is not observed in the dielectric spectra it is assigned to cooperative fluctuations in the alkyl side chain. As the alkyl side chain-rich domains are confined between the columns formed by the aromatic parts building molecules the α_2-relaxation can be characterized as hindered glass transition.[47] With increasing length of the alkyl side chain the size of the alkyl side chain-rich domains increases. This means, with increasing length of the side chain that the confinement effect is reduced and the α_2-rexation shifts to higher temperatures.

For the α_1-relaxtion polar groups must be involved as this process is observed by dielectric spectroscopy. Therefore, the α_1-realaxtion is assigned to either the aromatic core or the ionic head group of the building molecules which are self-assembled into columns. Currently no discrimination can be made between the two possibilities. A similar interpretation is made for other ILCs[21,22] as well as conventional columnar liquid crystals.[48–50] In principle this glass transition can be considered as a glass transition in a one-dimensional liquid.

Conductivity. As the DOPA*n* samples contain ions it is interesting to analyze the conductivity. The complex dielectric function is related to the complex conductivity $\sigma^*(\omega)$ by

$$\sigma^*(\omega) = \sigma'(\omega) + i\sigma''(\omega) = i\omega\varepsilon_0\varepsilon^*(\omega). \quad (6)$$

Here σ' and σ'' are real and imaginary part of the complex conductivity given by:

$$\sigma'(\omega) = \omega\varepsilon_0\varepsilon''(\omega) \quad (6a)$$

$$\sigma''(\omega) = \omega\varepsilon_0\varepsilon'(\omega) \quad (6b)$$

Fig. 8(b) depicts $\sigma'(f)$ *versus* frequency for the DOPA samples with different side chain length in the Col_h phase at comparable temperatures. The frequency dependence of $\sigma'(f)$ exhibits the distinctive behavior of semi-conductive materials. At high frequencies, $\sigma'(f)$ decreases with decreasing frequency, following a power law, until it reaches a plateau that characterizes the DC conductivity σ_{DC}. From a theoretical point of view the frequency dependence of $\sigma'(f)$ can be understood by the random barrier model.[51] The subsequent decrease in $\sigma'(f)$ at even lower frequencies is attributed to two different polarization effects Maxwell/Wagner/Sillars (MWS-) polarization at higher frequencies and electrode polarization at lower frequencies. The MWS-polarization is due to blocking of charge carriers at mesoscopic internal phase boundaries where electrode polarization is due to blocking of charge carriers at the electrodes.[36]

The DC conductivity is determined by fitting the Jonscher equation[52] to the frequency dependence $\sigma'(f)$, while excluding polarization effects. The Jonscher equation is expressed as

follows:

$$\sigma'(f) = \sigma_{DC}\left(1 + \left(\frac{f}{f_c}\right)^n\right) \quad (7)$$

The exponent n ranges between 0.5 and 1. The frequency f_c marks the onset of dispersion. The DC conductivity is related to f_c through the empirical Barton–Nakajima–Namikawa (BNN) relation.[36]

The DC conductivity is depicted *versus* inverse temperature in Fig. 9. With increasing temperature, the phase transition from the plastic crystalline to the hexagonally ordered liquid crystalline phase is observed as step-like change of σ_{DC} where in the plastic crystalline state the σ_{DC} is about two orders of magnitude lower than in the Col_h phase. A similar behavior was observed for ionic crystals.[53] This suppression of the DC conductivity at the phase transition was discussed by strong ion–ion correlations. A similar line of arguments can be applied here for the considered DOPA*n* ILCs. In the Col_h phase the charge transport is due to the drift motion of ions in the channels formed by the superdiscs. Therefore, the conductivity in the Col_h can be considered as ionic conductivity.

For the considered ILCs, at a fixed temperature the DC conductivity decreases with increasing length of the alkyl side chain in the plastic crystalline as well as in the Col_h phase. A similar behavior was observed for a related ILC.[23] Although it is expected that the charge transport takes place in the ion channels this result indicates that the alkyl side chains have some influence on the charge transport. Based on a quantitative analysis of X-ray measurements in confinement in ref. 23 it was discussed that with increasing length of the side chains some disorder as well as defects are introduced to the columns which leads to less defined ion channels resulting in a lower conductivity.

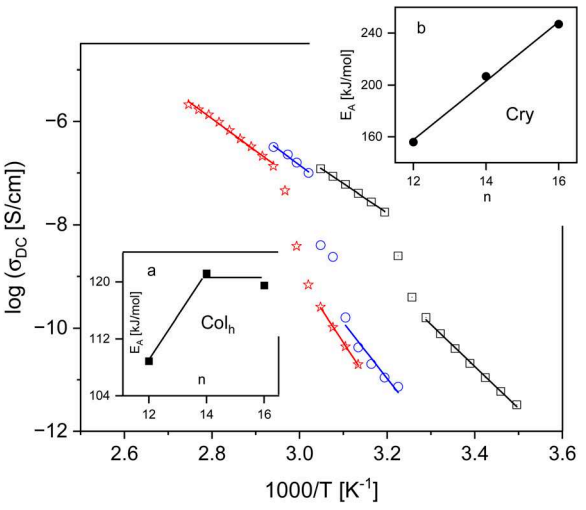

Fig. 9 DC conductivity *versus* inverse temperature in the Arrhenius diagram: black squares – DOPA12, blue circles – DOPA14 and red asterisk – DOPA16. Solid lines are fits of the Arrhenius equation to the corresponding data in the Col_h and in the plastic crystalline phase. Inset a – activation energy *versus* the number of the carbon atoms in the side chain in the Col_h phase. Lines are guides for the eyes. Inset b – activation energy *versus* the number of the carbon atoms in the side chain in the plastic crystalline phase. The line is a linear regression to the data.

The temperature dependence of the DC conductivity follows an Arrhenius dependence in the Cry as well as in the Col_h phase where the corresponding (apparent) activation energies are higher for the Cry state compared to the Col_h phases. This means that charge transport is more restricted in the plastic crystalline than in the hexagonal ordered liquid crystalline phase. The restriction of the charge transport in the plastic crystalline phase might be due to ion–ion correlations.[53] In the plastic crystalline phase, the activation energy for the DC conductivity increases approximately linearly with increasing length of the alkyl side chain (see inset b Fig. 9). In the hexagonal ordered liquid crystalline state the corresponding activation energy for σ_{DC} also increases strongly if the length of the side chain is increased from 12 to 14, reaching afterwards a plateau for longer length of the side chain (see inset b Fig. 9). Both results agree with the assumption that the ion channels become less defined with increasing side chain length. The less defined ion channels lead to a restriction of the charge transport and therefore to an increase of the activation energy for charge transport due to additional traps and obstacles, leading to a limitation of charge transport.

Confined samples

Phase behavior. Due to the available sample amount for confined samples DSC measurements in nanoconfinement could only be prepared for DOPA16. Fig. 10(a) depicts the heat flow *versus* temperature for DOPA16 confined in native AAO pores with a diameter of 180 nm and 80 nm in comparison to bulk DOPA16. In ref. 29 it was discussed that the liquid crystalline phase in confinement is not a Col_h phase but a nematic one. For native (hydrophilic) pore walls the phase transition from the plastic crystalline phase to the liquid crystalline states is observed as a peak with approximately the same maximum temperature. This is different for a comparable ILCs were a downshift of the phase transition temperature of *ca.* 8 K is observed when confined to pores with a diameter of 180 nm.[33] First, this difference can be due to the different aromatic core structure of the used ILCs. DOPA16 is based on an aromatic amino acid whereas the ILC discussed in ref. 33 has a phenyl benzoate core. It is also worth noting, that the ILC used in ref. 33 has an acyclic head group whereas DOPA16 has a cyclic one. Second, in ref. 29 it was discussed the mesophase formed by DOPA16 confined to pores with a dimeter of 180 nm is not a Col_h phase. Therefore, it might be not expected that the phase transition temperatures shift is a similar way. To discriminate between these rationales, additional investigations must be carried out. However, the peak is much broader compared to that of the phase transition in bulk, leading to a much lower onset temperature. Moreover, it is worth noting the crystal/crystal transition is not observed for confined DOPA16.

For DOPA16 confined to native pores with a pore diameter of 80 nm the phase transition from the plastic crystalline to the liquid crystalline state is downshifted by 2 K. This shift of the phase transition temperature to lower temperature is much smaller than that reported for the ILC with phenyl benzoate

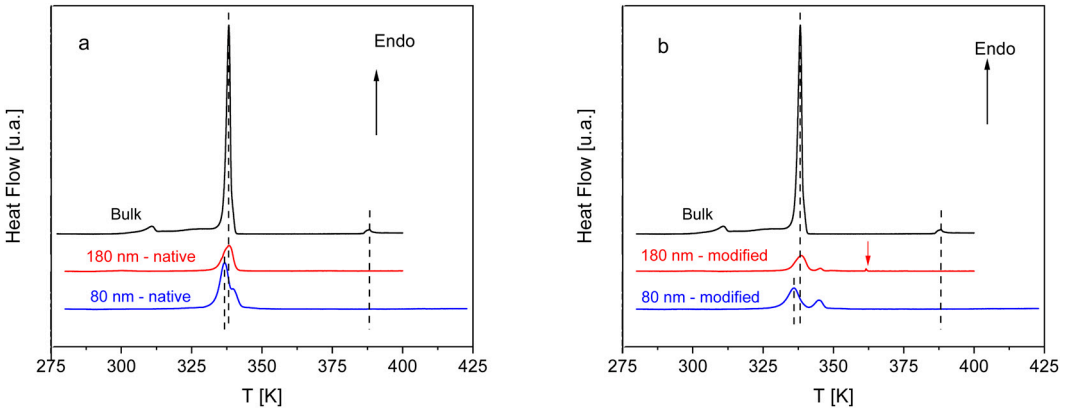

Fig. 10 (a) Heat flow *versus* temperature for DOPA16 confined to native pores at the given pore sizes: black – bulk, red – 180 nm, blue – 80 nm. (b) Heat flow *versus* temperature for DOPA16 confined to modified pores at the given pore sizes: black – bulk, red – 180 nm, blue – 80 nm. For all measurements the second heating run is analyzed. The heating rate was 5 K min^{-1}.

core.[33] Moreover, there seems to be a shoulder at the peak at higher temperatures which might indicate a second phase transition, which possibly is associated with DOPA16 adsorbed at the pore walls as this shoulder is not observed for the bulk state. Due to the interaction of the molecules with the pore walls a different structure of the ILC is formed which a higher phase transition temperature. It is worth noting that such a phase transition related to adsorbed material is not observed for the related ILC with the phenyl benzoate core. However, a similar behavior was found for the conventional discotic liquid crystal HAT6.[54]

The phase transition from Col_h phase to the isotropic state is not observed as a peak in the heat flow. This means this phase transition is suppressed in the thermal response. A similar behavior was observed for the corresponding ILC with phenyl benzoate core.[33] In ref. 33 this was discussed that the phase transition of the first order characteristic for the bulk is change to a continuous phase transition of the material confined in the pores. Nevertheless, it could not be completely excluded, that the thermal response at this phase transition is too weak to be detected by DSC.

Fig. 10(b) gives the heat flow *versus* temperature for DOPA16 confined to pores with modified (hydrophobic) pore wall. Like for the pores with native pore walls the phase transition from the plastic crystalline phase to the liquid crystalline phase is observed as a well-defined peak. For the pore with a diameter of 180 nm the phase transition takes place approximately at the same temperature as for the bulk. This behavior is also different from that for the corresponding liquid with phenyl benzoate core, where a shift to lower temperature by 7 K is observed.[33] For modified pores with a pore size of 80 nm the phase transition is shifted by *ca.* 3 K to lower temperatures. This downshift of the phase transition is by 1 K higher than for the native pore size but still much smaller than the corresponding ILC with the phenyl benzoate core.[33]

For DOPA16 confined to pores with modified pore walls the phase transition observed as a shoulder of the main peak is now observed as a separate peak at higher temperatures. This shift of the phase transition to higher temperatures supports its assignment to a second phase at the pore wall. The alkyl side chains of DOAP16 might interact with that of *n*-octadecylphosphonic acid and stabilize that phase leading to a higher phase transition temperature. For the DOPA16 confined to modified pores with a pore size of 80 nm the phase transition enthalpy is higher than that of DOPA16 embedded in modified pores with a diameter of 180 nm. This result supports the interpretation that the second peak is due to a phase transition of DOPA16 adsorbed at the pore wall. With decreasing pore size, the ratio of DOPA16 adsorbed at pore wall to that in the middle of the pores increases. The higher amount of adsorbed DOPA16 for pores with a pore size of 80 nm leads to a higher phase transition enthalpy.

Like with the native pore wall, the phase transition from the Col_h phase is not observed in the DSC measurements for DOPA16 confined in pores with modified pore walls. For DOPA16 embedded in modified pores with a pore size of 180 nm there is a further small peak observed in the heat flow. In the moment it is not clear whether this peak indicates a phase transition or if it is an artefact of the measurement.

Molecular mobility. Compared to the bulk the spectra for the confined samples in the temperature range of the α_1-relaxation is dominated by conductivity and polarization effects (see Fig. 11(a)). To analyze the data in such cases a so-called conduction free loss approach can be employed.[55] It could be shown that for a Debye relaxation process

$$\varepsilon''_{\mathrm{Deriv}} = -\frac{\pi}{2}\frac{\mathrm{d}\varepsilon}{\mathrm{d}\log\omega} = \varepsilon''^{2} \qquad (8)$$

holds. By this approach contributions to the conductivity due to Ohmic conduction are removed from the spectra. In addition, due to the square in eqn (8) the width of the conduction free loss is smaller than that of ε'' itself. The efficacy of this technique is illustrated in Fig. 11, which presents a comparative analysis of the frequency dependence of ε'' and $\varepsilon''_{\mathrm{Deriv}}$. A peak is observed in $\varepsilon''_{\mathrm{Deriv}}$ (see Fig. 11(b)). This peak indicating the relaxation process appears more pronounced in the derivative representation and is called α_3-relaxation. With increasing temperature, the α_3-relaxation shifts to higher frequencies as expected for a relaxation process.

Fig. 12(a) compares $\varepsilon''_{\mathrm{Deriv}}$ *versus* temperature at a frequency of 10 Hz for DOPA12 in the bulk and confined to pores with pore sizes of 180 nm and 25 nm having native pore walls. In this

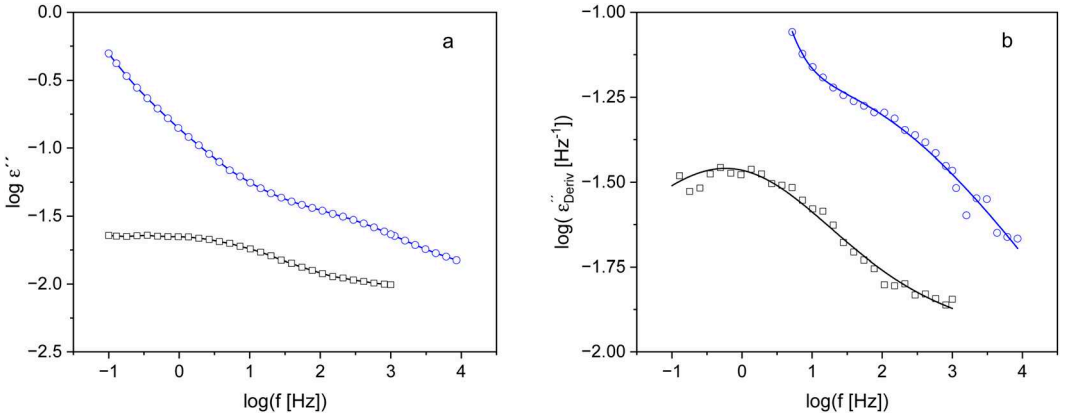

Fig. 11 (a) Dielectric loss *versus* frequency for DOPA12 confined to pores with a diameter of 180 nm with native pore walls: black squares – T = 262 K and blue circles – T = 298 K. Lines are guides for the eyes. (b) $\varepsilon''_{\mathrm{Deriv}}$ *versus* frequency for the same material and temperatures as given in part a. Lines are fits of eqn (9) to the data.

representation for the bulk DOPA12 the α_1-relaxation is observed as pronounced peak beside polarization effects. As shown in Fig. 11(b) for DOPA12 confined to pores with a pore size of 180 nm with native pore walls also shows a relaxation process, the α_3-relaxation. The α_3-relaxation is shifted by more than 70 K to higher temperatures compared to the α_1-relaxation of bulk DOPA12. No relaxation process is observed for bulk DOPA12 in the temperature range of α_3-relaxation. Further also no relaxation process is observed for confined DOPA12 in the temperature range of α_1-relaxation. Because of this large temperature shift it seems unlikely that the α_3-relaxation observed for confined DOPA12 is due to the α_1-relaxation observed for bulk DOPA12. Such a large shift would require a pronounced structural change of the DOPA12 ILC in confinement compared to that of the bulk which is not observed in the X-ray investigations.[29] Therefore it is concluded that the α_3-relaxation is induced by the confinement for instance by adsorption of DOPA12 molecules at the pore walls. The DSC measurements presented in Fig. 10 provide some evidence that such an adsorbed layer is formed and that this layer also undergoes a phase transition from the plastic crystalline to the $\mathrm{Col_h}$ phase. The reason why the α_1-relaxation is not observed for the confined samples remains unclear. It might be that the intensity becomes too low to be detected for the confined samples.

For DOPA12 confined to pores with a diameter of 25 nm with native pore wall the α_3-relaxation is shifted to even higher temperatures. Moreover, the α_3-relaxation appears more pronounced with a higher intensity compared to that of DOPA12 confined to native pores with a diameter of 180 nm. Both findings support the assignment of the α_3-relaxation to a process taking place in an adsorbed layer of DOPA12 molecules at the pore walls.

Fig. 12(b) compares $\varepsilon''_{\mathrm{Deriv}}$ *versus* temperature at a frequency of 10 Hz for DOPA*n* confined to pores with a diameter of 180 nm with native pore wall with different length. The α_3-relaxation shifts to higher temperatures for DOPA14 compared to that of DOPA12. For DOPA16 the α_3-relaxation is not observed. It might be that this does not exist for DOPA16 or that α_3-relaxation is hidden by the polarization effects. The former interpretation seems to be more likely as the α_3-relaxation is also not observed for confined DOPA16 at lower frequencies in the dielectric spectra. It might be argued that the long alkyl side chains of

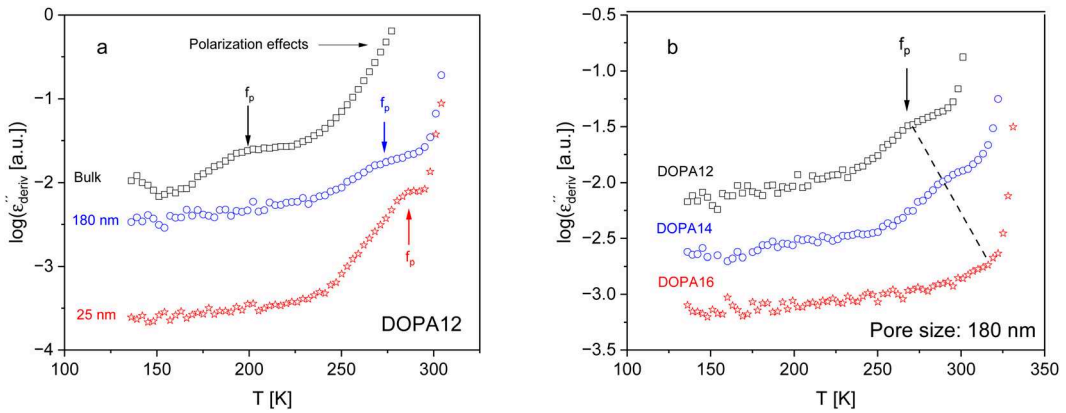

Fig. 12 (a) $\varepsilon''_{\mathrm{Deriv}}$ *versus* temperature at a frequency of 10 Hz for DOPA12: black squares – bulk, blue circles – 180 nm, red asterisk – 25 nm. The spectra are shifted along the y-scale for sake of clearness. All pores have native pore walls. (b) $\varepsilon''_{\mathrm{Deriv}}$ *versus* temperature for DOPA*n* confined to pores with a diameter of 180 nm with native pore walls at a frequency of 10 Hz: black squares – DOPA12, blue circles – DOPA14, red asterisk – DOPA16. The spectra are shifted along the y-scale for sake of clearness.

DOPA16 prevents the formation of an adsorbed layer. Further is might be also argued that for DOPA16 in confinement no Col_h phase but may be a nematic ones is observed by synchrotron-based X-ray scattering.[29] Thus it might be discussed that the α_3-relaxation does not occur in a nematic phase.

For DOPA12 confined to native pores with a diameter of 25 nm the α_3-relaxation could be observed. This is not the case for DOPA12 confined to modified pores with the same pore size of 25 nm. It might be discussed that the alkyl chains of DOPA12 interfere with that of ODPA and prevent the formation of an adsorbed layer.

For DOPA14 the α_3-relaxation could be only observed when confined to native pores with a diameter of 180 nm. For modified pores with a size of 180 nm and for DOPA14 confined to pores of 25 nm no α_3-relaxation could be detected. Again, it can be discussed that the longer alkyl side chains of DOPA14 in comparison to DOPA12 prevents the formation of an adsorbed layer.

To analyze the frequency dependence of ε''_{Deriv} the derivative of the real part of the Havriliak–Negami function, $\frac{d\varepsilon'_{HN}}{d\log\omega}$, is fitted to the data. The expression for $\frac{d\varepsilon'_{HN}}{d\log\omega}$ is given by

$$-\frac{d\varepsilon'_{HN}}{d\log\omega}=\frac{1}{\ln(10)}\frac{\beta\gamma\Delta\varepsilon_{HN}(\omega\tau_{HN})^{\beta}\cos\left(\frac{\beta\pi}{2}\right)(-(1+\gamma)\Psi(\omega))}{\left[1+2(\omega\tau_{HN})^{\beta}\cos\left(\frac{\beta\pi}{2}\right)+(\omega\tau_{HN})^{2\beta}\right]^{\frac{1+\gamma}{2}}} \quad (9a)$$

with

$$\Psi(\omega)=\arctan\left[\frac{\sin\left(\frac{\beta\pi}{2}\right)}{(\omega\tau_{HN})^{-\beta}+\cos\left(\frac{\beta\pi}{2}\right)}\right]. \quad (9b)$$

To describe remaining polarization effects, a power law $\sim\omega^{-n}$ was added to eqn (9a). Examples for the fitting process of $\frac{d\varepsilon'_{HN}}{d\log\omega}$ to the data of DOPA12 confined to pores with a diameter of 180 nm having native pore walls are depicted in Fig. 11(b).

Fig. 13(a) depicts the relaxation map for DOPA12 confined to native pores with a diameter of 180 nm and 25 nm and pores with modified pore walls with a diameter of 180 nm. As discussed above the α_3-relaxation is shifted by more than 70 K to higher temperatures compared to the α_1-relaxation as well as more than 50 K compared the α_2-relaxation. The temperature dependence of the relaxation rates of the α_3-relaxation can be described by the VFT equation. This temperature dependence might imply that the α_3-relaxation is a dynamic glass transition. The temperature dependence of the α_3-relaxation of DOPA12 confined to pores with a diameter of 25 nm with native walls are shifted by *ca.* 20 K to higher temperature compared to DOPA12 embedded in pores with a diameter of 180 nm also with native pore surfaces. This shift in the temperature dependence indicates a further confinement effect on the molecular dynamics of DOPA12 in the adsorbed layer. Moreover, the curvature of the temperature dependence for DOPA12 confined to pores with a diameter of 25 nm is higher than that of DOPA12 confined to pores with a diameter of 180 nm. This means the glassy dynamics is more fragile for the surface layer in pores with a diameter of 25 nm than for pores with a diameter of 180 nm.

Unfortunately, for DOPA12 confined to pores with a diameter of 180 nm with modified pore walls only a few points could be estimated for the α_3-relaxation. These few points might indicate that the α_3-relaxation in the pores with modified pore surfaces is shifted further to higher temperatures. This temperature shift seems to indicate the involvement of the alkyl chains of ODPA in the α_3-relaxation. Moreover, for the modified

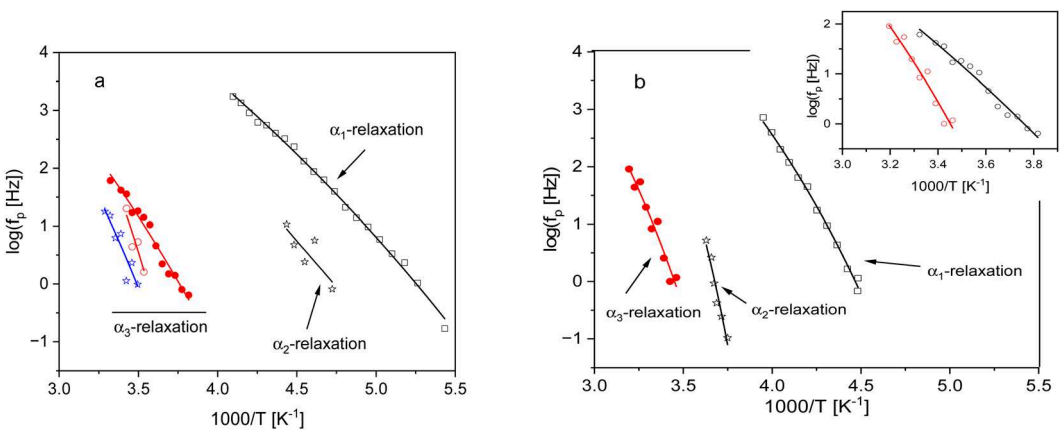

Fig. 13 (a) Relaxation rate *versus* temperature for bulk and confined DOPA12: black squares – α_1-relaxation for the bulk, black asterisk – α_2-relaxation for the bulk, red solid circles- confined to pores with a diameter of 180 nm with native pore walls, red open circles – confined to pores with a diameter of 180 nm with modified pore walls, blue asterisk – confined to pores with a diameter of 25 nm with native pore walls. Lines are fits of the VFT equation to the corresponding data. (b) Relaxation rate *versus* temperature for bulk and confined DOPA14: black squares – α_1-relaxation for the bulk, black asterisk – α_2-relaxation for the bulk, red solid circles-confined to pores with a diameter of 180 nm with native pore walls. Lines are fits of the VFT equation to the corresponding data. The inset compares the temperature dependence of the α_3-relaxation of DOPA*n* confined to pores with a diameter of 180 nm with native pore walls: black circles – DOPA12 and red circles – DOPA14. Lines are fits of the VFT equation to the corresponding data.

pores the α_3-relaxation seems to be more fragile than that in native pores.

Fig. 13(b) gives the relaxation map for DOPA14 confined to native pores with a diameter of 180 nm. At a frequency of 10 Hz the α_3-relaxation is observed at a temperature *ca.* 66 K higher than the α_1-relaxation and at a temperature 18 K higher than the α_2-relaxation. These temperature differences are a bit smaller than that observed for DOPA12. Nevertheless, temperature differences are also large and supports the line of argumentation that the molecular origin of α_3-relaxation is induced by the confinement and is most likely a relaxation due to an adsorbed layer.

The inset of Fig. 13(b) compares the temperature dependence of the α_3-relaxation of DOPA12 and DOPA14 confined to pores with a diameter of 180 nm with native pore walls. As discussed above the α_3-relaxation for DOPA14 is shifted to higher temperatures compared to that of DOPA12. Moreover, the α_3-relaxation for DOPA14 seems to be more fragile than that of DOPA12. Both results support the involvement of the alkyl side chains in the α_3-relaxation.

Conductivity. To discuss the conductivity for the confined samples one must consider the measured equivalent circuit is a combination of the ILC in the channels in the AAO membrane and the membrane itself. As the channels are parallel to the employed electrical field it is a parallel circuit. The measured conductivity σ^*_{obs} for the confined samples is scaled by the porosity:

$$\sigma^*(f) = \frac{\sigma^*_{obs}(f)}{\text{porosity}} \tag{10}$$

Fig. 14(a) compares the frequency dependence of the real part of the complex conductivity for bulk DOPA12 and confined to native pores with diameters of 180 nm and 25 nm at 319 K. As discussed above for bulk DOPA12 the frequency dependence of the real part of the conductivity follows the typical pattern: a decrease with decreasing frequency according to a power law, followed by a plateau indicating the DC conductivity. At even lower frequencies, polarization effects are observed as a further decrease in the real part of the conductivity. For confined DOPA12 the real part of the complex conductivity is more complex as $\sigma'(f)$ shows a two-step decay with decreasing frequency and a plateau at lowest frequencies. The simplest interpretation might be to attribute the step-like decay of $\sigma'(f)$ with decreasing frequencies to polarization effects. However, the onset of polarization effects should be accompanied by a minimum in the frequency dependence in the imaginary part of the complex conductivity.[56] Such a minimum is observed for bulk DOPA12 (see Fig. S3). A minimum in $\sigma''(f)$ is also observed for DOPA12 embedded in pores with a diameter of 180 nm but at much lower frequencies than the step-like decay observed in $\sigma'(f)$. No minimum is observed in the frequency dependence of σ'' for DOPA12 confined to native pores with a diameter of 25 nm. Therefore, it is concluded that the step-like decay observed for $\sigma'(f)$ is not due to polarization effects. A similar behavior is also observed for confined DOPA14 and DOPA16.

To elucidate the problem further, the conduction free loss is considered in Fig. 14(b) at the same temperature as the conductivity in Fig. 14(a). For bulk DOPA12 ε''_{Deriv} shows that at the first glance only polarization effects are found where for confined DOPA12 a peak is observed indicating a dielectric active process with Debye-like shape. Such a process can have different origins. Firstly, in ref. 28 such a process is assigned to the exchange of building molecules between adjacent superdiscs due to defects of it. However, this process is not directly observed for bulk DOPA*n*. It might be that it is hidden by the polarization effects because it has a weaker intensity in bulk, as the columns have less defects in the bulk.

Secondly, recently a so-called slow Arrhenius process (SAP)[57,58] was discussed for a conventional discotic liquid crystal in ref. 59. It might be that the process observed here for the confined DOPA*n* materials corresponds also to a SAP.

Thirdly, although the pores are completely filled, there might be a meniscus at the openings of the channels. The meniscus will cause an air capacitor in series with the material

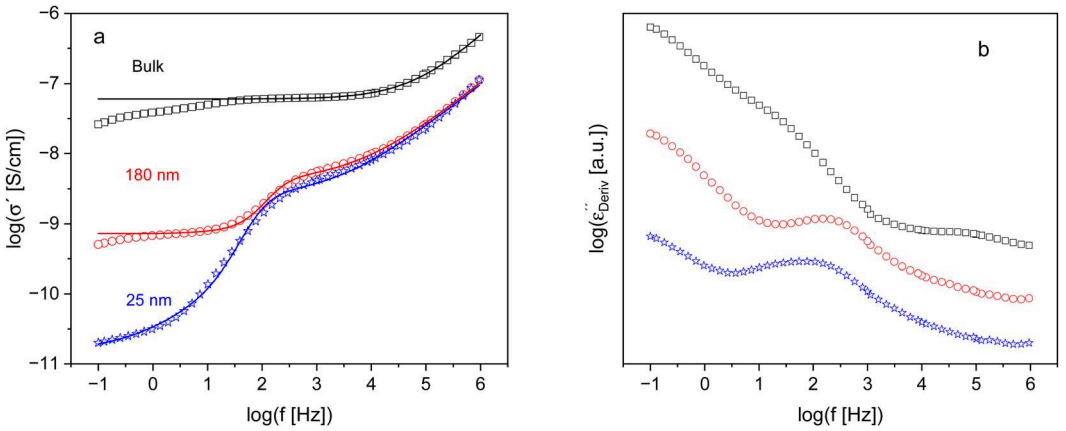

Fig. 14 (a) Real part of the complex conductivity *versus* frequency at a temperature of 319 K: back squares – bulk DOPA12, red circles – confined to native pores with a diameter of 180 nm and blue asterisk – confined to native pores with a diameter of 25 nm. The black line is a fit of eqn (7) to the data of bulk DOPA12. The blue and red lines are fits of eqn (11) to the data of confined DOPA12. (b) ε''_{Deriv} *versus* frequency for DOPA12 at T = 319 K: black squares – bulk; red circles – confined to native pores with a diameter of 180 nm and blue asterisk – confined to native pores with a diameter of 25 nm. The curves are shifted along the *y*-scale for the sake of clarity.

in the channels. The equivalent circuit of two serial capacitors will lead to a parasitic process even in the case where no time dependent process takes place in the two capacitors.[36]

Currently it cannot be differentiated between the three interpretation possibilities. Therefore, this process is not considered further. Nevertheless, it must be taken into consideration during the analysis of the conductivity. Therefore, the Jonscher equation (eqn (7)) is extended by adding a Debye-process to describe $\sigma'(f)$. The complete fit function reads

$$\sigma'(f) = \sigma_{DC}\left(1 + \left(\frac{f}{f_c}\right)^n\right) + \frac{\frac{f^2}{f_{proc}}\Delta\sigma}{1 + \left(\frac{f}{f_{proc}}\right)^2} \quad (11)$$

Here f_{proc} is the rate of the additional process and $\Delta\sigma$ is a fitting parameter related to the dielectric intensity of that process. Fig. 14(a) shows that this procedure captures the frequency dependence of the real part of the complex conductivity for the confined samples.

Fig. 15 depicts the DC conductivity *versus* inverse temperature for all confined samples in comparison to the corresponding bulk. As a first result for all DOPA*n* materials in nanoscale confinement the DC conductivity is lower than that of the bulk for all mesophases. Moreover, for confined DOPA12 and DOPA14 the phase transition from the isotropic to the Col_h is detected as a change in the temperature dependence of σ_{DC}. For all confined DOPA*n* materials the phase transition from the liquid crystalline state is further monitored by a change in the temperature dependence of the DC conductivity.

It is expected that the conductivity of DOPA*n* ILCs depends on the orientation of the superdiscs in the nanopores. Therefore, the possible orientation of the superdiscs in cylindrical nanopores will be shortly discussed. At planar surfaces columnar liquid crystals can have two kinds of orientation: the face-on (homeotropic) orientation or the edge on (planar or homogeneous) anchoring. In cylindrical nanopores a variety of different orientations or textures can be observed. These orientation consist of the radial, logpile, circular concentric and the axial orientation.[29,60–64] The kind of orientation depends on hydrophobicity of the pore wall and the ILC (alkyl side chain length) as well as on the pore size. In the following the DC conductivity for each material will be separately discussed only for the liquid crystalline state.

Confined DOPA12. For the discussion of the σ_{DC} in confinement one has to keep in mind that in general the DC conductivity is the product of the number of the charge carriers and its mobility. For DOPA12 confined to native (hydrophilic) pores with a diameter of 180 nm the DC conductivity in the Col_h phase (T = 324 K) is by *ca.* 1.7 orders of magnitude lower that in the bulk state (see Fig. 15(a)). Firstly, this can be

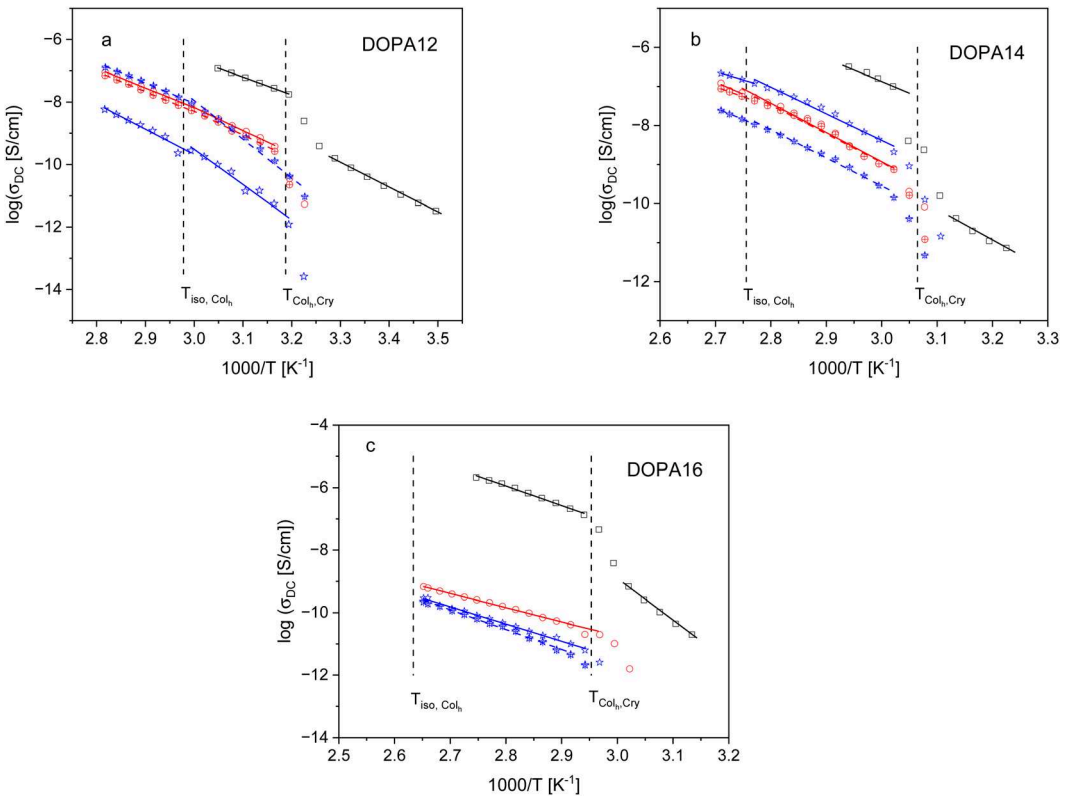

Fig. 15 DC conductivity *versus* inverse temperature for the confined DOPA*n* samples in comparison to the bulk state. Squares – bulk; red circles – confined to native pores with a pore diameter of 180 nm; red crossed circles – confined to modified pores with a pore diameter of 180 nm; blue asterisk – confined to native pores with a pore diameter of 25 nm and blue crossed asterisk – confined to modified pores with a pore diameter of 25 nm. Lines are linear regression to the corresponding data in the different temperature ranges.

discussed as a confinement effect on the conductivity. Secondly, in ref. 29 it was revealed for DOPA12 confined in native pores with a diameter of 180 nm that the superdiscs are aligned radial to the long axis of the pores. This includes that parts of the superdiscs are aligned in perpendicular to the long channel axis. In the following one has to consider that the charge transport in columnar ILCs takes place along the ion channels formed in the Col_h phase and that the electrical field is oriented in parallel to the pore axis. This means that for a partial perpendicular orientation of the superdiscs regarding the long axis of the pores, the mobility of the charge carriers in the direction of the pores is lower than that in the bulk. Further the activation energy of σ_{DC} in the Col_h phase of DOPA12 confined to native pores with a diameter of 180 nm is higher than that in the bulk. This result indicates that the charge transport is restricted in the pores compared to the bulk.

Although the Col_h phase is not found by birefringence measurements in ref. 29 for DOPA12 confined in modified pores it is observed in the dielectric measurements (see Fig. 15(a)). This difference in the results might be due to the different heating rates used in both experiments (1 K min^{-1} in the X-ray scattering and 0.1 K min^{-1} in the dielectric experiment). For DOPA12 confined to modified (hydrophobic) pores the conductivity is almost like that of DOPA12 embedded in hydrophilic (native) ones. Therefore, it is concluded, that the orientation of the superdiscs of DOPA12 confined in hydrophobic pores is like that in hydrophilic ones.

For DOPA12 confined in native pores with a diameter of 25 nm the DC conductivity at T = 324 K is further reduced by another *ca.* 1.7 orders of magnitude compared to that of DOPA12 embedded in native pores with a diameter of 180 nm (see Fig. 15(a)). At the first glance as a further confinement effect compared to native pores with a pore diameter of 180 nm. However, as for the superdiscs confined to pores with a diameter of 180 nm only a partial orientation perpendicular to the long axis of the pores was observed it might be further concluded that they orient further to perpendicular alignment with respect to the long axis of the channels. This point will become clearer in the next section. In addition, the activation energy of the DC conductivity for confined DOPA12 to native pores with a size of 25 nm is higher than for the corresponding case with a pore diameter of 180 nm. The higher activation energy indicates a further restriction of the charge transport in native pores with a diameter of 25 nm.

For DOPA12 confined to hydrophobic (modified) pores with a diameter of 25 nm the DC conductivity is by *ca.* 1.7 orders of magnitude higher than for the hydrophilic pores with the same diameter. As the confinement should be similar for both pore walls this result suggest a change in the orientation of the superdiscs from a more perpendicular to a more parallel one with respect to the long axis of the channels. It should be noted that the decrease of the conductivity for DOPA12 embedded in native pores with a diameter of 25 nm compared to the modified ones is not only a confinement effect but that the DC conductivity depends also on the orientation or alignment of the superdiscs in the pores.

Confined DOPA14. The DC conductivity for confined DOPA14 in comparison to the bulk is predicted in Fig. 15(b). For DOPA14 confined to pores with 180 nm having native pore walls the DC conductivity at T = 337 K is *ca.* two orders of magnitude lower than in the bulk. This is a bit more than for DOPA12 confined to the same pores. In ref. 29 a radial orientation of the superdiscs with regard the long axis of the pores is reported. Like for a perpendicular orientation the charge transport in the direction of the long channel axis is limited for this orientation of the superdiscs. Therefore, the σ_{DC} is reduced in comparison to the bulk due to the orientation of the superdiscs in addition to confinement effects. For the DOPA14 confined in hydrophobic pores with a diameter of 180 nm changed from a radial one to a concentric one.[29] For this orientation the charge transport cannot take place in the direction of the long channel axis. For that reason, the DC conductivity is similar than that in the hydrophilic pores with the same diameter.

Surprisingly for DOPA14 embedded in hydrophilic pores with a diameter of 25 nm σ_{DC} is higher than that for pores with a diameter of 180 nm with the same pore walls. This increase in the conductivity can be understood by a partly change in the orientation of the superdiscs from a radial orientation to a parallel one. This is further supported by the observation that the activation energy for hydrophilic pores with a diameter of 25 nm is lower than that of hydrophilic pores with the size of 180 nm.

For DOPA14 embedded in hydrophobic pores with a diameter of 25 nm at 337 K the DC conductivity is more than one order of magnitude lower than that in hydrophilic ones with the same pore size. Again, this can be understood by a change of the orientation of the superdiscs to a more perpendicular one regarding to the long axis of the channels. This conclusion is supported by the result that the activation energy of σ_{DC} for DOPA14 in hydrophobic pores with a diameter of 25 nm is higher than that for the hydrophilic pores. The different behavior observed for DOPA14 confined to pores with a diameter of 25 nm compared to that of DOPA12 might be due to the increased hydrophobicity of DOPA14 due to the longer alkyl side chain.

Confined DOPA16. The DC conductivity of confined DOPA16 in comparison to the bulk is given in Fig. 15(c). For DOPA16 embedded in hydrophilic pores with a diameter of 180 nm the DC conductivity at 352 K in the liquid crystalline state is by more than 3.8 orders of magnitude lower than that in the Col_h phase of the bulk. The observed change in the conductivity is much larger than that of DOPA12 and DOPA14 confined to the same pores. In ref. 29 it was found that the liquid crystalline state of DOPA16 changed from a Col_h phase to a nematic one. For nematic state no columns exist and a charge transport along ion channels cannot be expected. Most probably the conduction mechanism changes for a transport in ion channels of the bulk state changed to an ion hoping process in the confined state. Therefore, the DC conductivity is orders of magnitudes lower than for a Col_h state. As a nematic state has a lower order than that of the Col_h. For that reason, the activation for σ_{DC} is lower than that in the bulk.

For DOPA16 confined to hydrophilic and hydrophobic pores with a diameter of 25 nm the conductivity slightly decreases further, respectively where also the activation energy for charge transport increases.

Conclusion

This study provides a comprehensive analysis of the molecular mobility, phase behavior, and ionic conductivity of dopamine-based ionic liquid crystals (DOPA*n*, n = 12, 14, 16) in both the bulk state and under nanoconfinement within anodic aluminum oxide (AAO) membranes. By systematically varying the alkyl side chain length and employing advanced techniques such as broadband dielectric spectroscopy (BDS), differential scanning calorimetry (DSC), and fast scanning calorimetry (FSC), the complex interplay between molecular structure, self-assembly, and dynamic behavior in these systems was elucidated.

In the bulk state, DOPA*n* materials exhibit a well-defined phase sequence from plastic crystalline (Cry) to hexagonal columnar (Col_h) and finally to the isotropic (Iso) phase in order of increasing temperature. The formation of superdiscs by the conical building molecules through ionic interactions and their subsequent assembly into one-dimensional columns enables the formation of the Col_h phase. The space between the columns is filled by the alkyl side chains. This can be considered as nanosegregated structure consisting of the columns formed by the aromatic parts as well as the ionic head groups of the molecules and alkyl side chain-rich domains between in the intercolumnar space. The molecular mobility in the bulk reveals several relaxation processes: the γ-relaxation associated with localized fluctuation in the side chains, the α_1-relaxation linked to the ionic headgroup or aromatic core, and the α_2-relaxation attributed to cooperative dynamics within the alkyl-rich domains. The α_1-relaxation and the α_2-relaxation are considered as different glassy dynamics related to a glass transition. The DC conductivity is significantly higher in the Col_h phase than in the Cry state. Presumably the mechanism for charge transport in the Col_h state is a diffusion of ions along in ion channels. The conductivity decreases as the alkyl chain length increases – likely due to an increased disorder and defect density within the columns forming the ion channels.

Under nanoconfinement, the behavior of DOPA*n* deviates markedly from the bulk behavior. The phase transition from Col_h to Iso is suppressed, and the transition from Cry to the liquid crystalline state becomes broader and shifts slightly depending on pore size and surface chemistry. Notably, a new relaxation process (α_3-relaxation) emerges, absent in the bulk, which is attributed to dynamic processes within an adsorbed layer at the pore walls. This relaxation is highly sensitive to pore diameter, surface hydrophobicity, and alkyl chain length, indicating a confinement-induced dynamic glass transition.

The DC conductivity of confined DOPA*n* is consistently lower than in the bulk, with reductions spanning up to nearly four orders of magnitude for DOPA16. This suppression is influenced not only by the spatial confinement but also by the orientation of the superdiscs within the pores and a change of the mesophase type. For instance, perpendicular or radial alignment relative to the pore axis hinders charge transport along the electric field direction along the long axis of the columns. In the case of DOPA16, confinement induces a phase change from Col_h to a nematic-like state, fundamentally altering the conduction mechanism from ion channel transport to ion hopping, thereby drastically reducing conductivity.

In summary, this work highlights the profound impact of nanoscale confinement on the structural and dynamic properties of ionic liquid crystals. The findings underscore the importance of molecular design, pore architecture, and surface chemistry in tailoring the performance of ILCs for applications in material science like nanofluids, ion transport, biology, and responsive materials.

Conflicts of interest

There are no conflicts to declare.

Data availability

Data will be available from the corresponding author on a reasonable request.

Polarized optical microscopy. XRD pattern, Imaginary part of the complex dielectric conductivity. See DOI: **https://doi.org/10.1039/d5cp02406d**

Acknowledgements

The financial support by the German Research Foundation (DFG Project number 430146019 – SCHO 470/26-1, HU 850/13-1, LA 907/21-1) is acknowledged.

References

1 S. Laschat, A. Baro, N. Steinke, F. Giesselmann, C. Hägele, G. Scalia, R. Judele, E. Kapatsina, S. Sauer, A. Schreivogel and M. Tosoni, Discotic Liquid Crystals: From Tailor-Made Synthesis to Plastic Electronics, *Angew. Chem., Int. Ed.*, 2007, **46**, 4832–4887.
2 N. Kapernaum, A. Lange, M. Ebert, M. A. Grunwald, C. Haege, S. Marino, A. Zens, A. Taubert, F. Giesselmann and S. Laschat, Current Topics in Ionic Liquid Crystals, *ChemPlusChem*, 2022, **87**, e202100397.
3 K. Goossens, K. Lava, C. W. Bielawski and K. Binnemans, Ionic Liquid Crystals: Versatile Materials, *Chem. Rev.*, 2016, **116**, 4643–4807.
4 A. F. M. Santos, J. L. Figueirinhas, M. Dionisio, M. H. Godinho and L. C. Branco, Ionic liquid crystals as chromogenic materials, *Materials*, 2024, **17**, 4563.
5 K. Salikolimi, A. A. Sudhakar and Y. Ishida, Functional Ionic Liquid Crystals, *Langmuir*, 2020, **36**, 11702–11731.
6 S. J. Devaki and R. Sasi, Ionic Liquids/Ionic Liquid Crystals for Safe and Sustainable Energy Storage Systems, in *Progress*

and Developments in Ionic Liquids, ed. S. Handy, *IntechOpen*, 2017, ch. 14.

7 S. Chen and S. H. Eichhorn, Ionic Discotic Liquid Crystals, *Isr. J. Chem.*, 2012, **52**, 830–843.

8 T. Onuma, E. Hosono, M. Takenouchi, J. Sakuda, S. Kajiyama, M. Yoshio and T. Kato, Noncovalent Approach to Liquid-Crystalline Ion Conductors: High-Rate Performances and Room-Temperature Operation for Li-Ion Batteries, *ACS Omega*, 2018, **3**, 159–166.

9 R. Sasi, S. Sarojam and S. J. Devaki, High Performing Biobased Ionic Liquid Crystal Electrolytes for Supercapacitors. ACS Sustainable, *Chem. Eng.*, 2016, **4**, 3535–3543.

10 D. Högberg, B. Soberats, R. Yatagai, S. Uchida, M. Yoshio, L. Kloo, H. Segawa and T. Kato, Liquid-Crystalline Dye-Sensitized Solar Cells: Design of Two-Dimensional Molecular Assemblies for Efficient Ion Transport and Thermal Stability, *Chem. Mater.*, 2016, **28**, 6493–6500.

11 K. S. Egorova and V. P. Ananikov, Toxity of Inonic Liquid Crystals: Eco(cyto)activity as complicated, but unavoidable parameter for task-specific optimization, *ChemSusChem*, 2014, **7**, 336–360.

12 J. Pernak, B. Legosz, F. Walkiewicz, T. Klejdysz, A. Borkowski and L. Chrzanowski, Ammonium ionic liquids with anions of natural origin, *RSC Adv.*, 2015, **5**, 65471–65480.

13 J. Gravel and A. R. Schmitzer, Imidazolium and benzimidazolium-containing compounds: from simple toxic salts to highly bioactive drugs, *Org. Biomol. Chem.*, 2017, **15**, 1051–1071.

14 M. A. Grunwald, S. E. Hagenlocher, L. Turkanovic, S. M. Bauch, S. B. Wachsmann, L. A. Altevogt, M. Ebert, J. A. Knöller, A. R. Raab, F. Schulz, M. A. Kolmangadi, A. Zens, P. Huber, A. Schönhals, U. Bilitiewski and S. Laschat, Does thermotropic liquid crystalline self-assembly control biological activity in amphiphilic amino acids? – Tyrosine ILCs as a case study, *Phys. Chem. Chem. Phys.*, 2023, **25**, 17639–17656.

15 M. Neidhardt, K. Schmitt, A. Baro, C. Schneider, U. Bilitewski and S. Laschat, Self-assembly and biological activities of ionic liquid crystals derived from aromatic amino acids, *Phys. Chem. Chem. Phys.*, 2018, **20**, 20371–20380.

16 S. Klembt; S. Dreyer; M. Eckstein and U. Kragl, In Ionic Liquids in *Synthesis*, ed. P. Wasserscheid and T. Welton, Wiley-VCH, Weinheim, 2nd edn, 2008, vol. 2, pp. 641–662.

17 S. Kumar, Discotic Liquid Crystal-Nanoparticle Hybrid Systems. NPG Asia, *Materials*, 2014, **6**, E82.

18 K. Goossens, K. Lava, C. W. Bielawski and K. Binnemans, Ionic Liquid Crystals: Versatile Materials, *Chem. Rev.*, 2016, **116**, 4643–4807.

19 Y. Ishii, N. Matubayasi, G. Watanabe, T. Kato and H. Washizu, Molecular Insights on Confined Water in the Nanochannels of Self-Assembled Ionic Liquid Crystal, *Sci. Adv.*, 2021, **7**, eabf0669.

20 M. Yoshio, T. Mukai, H. Ohno and T. Kato, One-Dimensional Ion Transport in Self-Organized Columnar Ionic Liquids, *J. Am. Chem. Soc.*, 2004, **126**, 994–995.

21 A. Yildirim, P. Szymoniak, K. Sentker, M. Butschies, A. Bühlmeyer, P. Huber, S. Laschat and A. Schönhals, Dynamics and Ionic Conductivity of Ionic Liquid Crystals Forming a Hexagonal Columnar Mesophase, *Phys. Chem. Chem. Phys.*, 2018, **120**, 5626–5635.

22 M. A. Kolmangadi, A. Yildirim, K. Sentker, M. Butschies, A. Bühlmeyer, P. Huber, S. Laschat and A. Schönhals, Molecular Dynamics and Electrical Conductivity of Guanidinium Based Ionic Liquid Crystals: Influence of Cation Headgroup Configuration, *J. Mol. Liq.*, 2021, **330**, 115666.

23 M. A. Kolmangadi, G. J. Smales, L. ZhuoQing, A. Yildirim, E. Wuckert, S. Eutionnat, F. Demel, P. Huber, S. Laschat and A. Schönhals, Side Chain Length-Dependent Dynamics and Conductivity in Self-Assembled Ion Channels, *J. Phys. Chem. C*, 2022, **126**, 10995–11006.

24 M. A. Kolmangadi, Y. M. Wani, A. Schönhals and A. Nikoubashman, Coarsed-Grained Simulations of Columnar Ionic Liquid Crystals: Comparison with Experiments, *J. Chem. Phys. B*, 2024, **128**, 8215–8222.

25 W. Tu, K. Jurkiewicz and K. Adrjanowicz, Confinement of pyrrolidinium-based ionic liquids [CnMPyrr] + [Tf2N]$^-$ with long cationic alkyl side chains (n = 10 and 16) to nanoscale pores: Dielectric and calorimetric studies, *J. Mol. Liq.*, 2021, **324**, 115115.

26 C. Grigoriadis, H. Duran, M. Steinhart, M. Kappl, H.-J. Butt and G. Floudas, Suppression of Phase Transitions in a Confined Rodlike Liquid Crystal, *ACS Nano*, 2011, **5**, 9208–9215.

27 C. Krause and A. Schönhals, Phase Transitions and Molecular Mobility of a Discotic Liquid Crystal under Nanoscale Confinement, *J. Phys. Chem. C*, 2013, **117**, 19712–19720.

28 M. A. Kolmangadi, L. Zhuoqing, G. J. Smales, B. R. Pauw, E. Wuckert, A. Raab, S. Laschat, P. Huber and A. Schönhals, Confinement-suppressed phase transition and dynamic self-assembly of ionic superdiscs in ordered nanochannels: Implication for nanoscale applications, *ACS Appl. Nano Mater.*, 2023, **6**, 15673–15684.

29 Z. Li, A. Raab, M. A. Kolmangadi, M. Busch, M. Grunwald, F. Demel, F. Bertram, A. V. Kityk, A. Schönhals, S. Lachat and P. Huber, Self-Assembly of Ionic Superdiscs in Nanopores, *ACS Nano*, 2024, **18**, 14414–14426.

30 M. Butschies, J. C. Haenle, S. Tussetschläger and S. Laschat, Liquid Crystalline Guanidinium Phenylalkoxybenzoates: Towrds Room Temperature Liquid Crystals via Bending of the Mesogenic Core and he Use of Triflate Counterions, *Liq. Cryst.*, 2013, **40**, 52–71.

31 C. Krause, R. Zorn, F. Emmerling, J. Falkenhagen, B. Frick, P. Huber and A. Schönhals, Vibrational density of states of triphenylene based discotic liquid crystals: dependence on the length of the alkyl chain, *Phys. Chem. Chem. Phys.*, 2024, **16**, 7324–7333.

32 C. Grigoriadis, H. Duran, M. Steinhart, M. Kappl, H.-J. Butt and G. Floudas, Suppression of Phase Transitions in a Confined Rodlike Liquid Crystal, *ACS Nano*, 2011, **5**, 9208–9215.

33 M. A. Kolmangadi, L. Zhuoqing, G. J. Smales, B. R. Pauw, E. Wuckert, A. Raab, S. Laschat, P. Huber and A. Schönhals, Confinement-suppressed phase transition and dynamic self-assembly of ionic superdiscs in ordered nanochannels: Implication for nanoscale applications, *ACS Appl. Nano Mater.*, 2023, **6**, 15673–15684.

34 V. Mathot, M. Pyda, T. Pijpers, G. Vanden Poel, E. van de Kerkhof, S. van Herwaarden, F. van Herwaarden and A. Leenaers, The Flash DSC 1, a Power Compensation Twin-Type, Chip-Based Fast Scanning Calorimeter (FSC): First Findings on Polymers, *Thermochim. Acta*, 2011, **522**, 36–45.
35 S. Havriliak and S. Negami, A Complex Plane Analysis of α-Dispersions in Some Polymer Systems, *J. Polym. Sci., Part C: Polym. Symp.*, 1966, **14**, 99–117.
36 A. Schönhals and F. Kremer, Analysis of Dielectric Spectra, in *Broadband Dielectric Spectroscopy*, ed. F. Kremer and A. Schönhals, Springer, Berlin, Heidelberg, 2003, pp. 59–98.
37 O. van den Berg, W. G. F. Sengers, W. F. Jager, S. J. Picken and M. Wübbenhorst, Dielectric and Fluorescent Probes To Investigate Glass Transition, Melt, and Crystallization in Polyolefins, *Macromolecules*, 2004, **37**, 2460–2470.
38 J. C. Dyre, A phenomenological model for the Meyer–Neldel rule, *J. Phys. C: Solid State Phys.*, 1986, **19**, 5655.
39 A. Yelon, B. Movaghar and H. M. Branz, Origin and consequences of the compensation (Meyer-Neldel) law, *Phys. Rev. B: Condens. Matter Mater. Phys.*, 1992, **B46**, 12244.
40 E. Thoms and S. Napolitano, Enthalpy-entropy compensation in the slow Arrhenius process, *J. Chem. Phys.*, 2023, **159**, 161103.
41 A. Schönhals, D. Wolff and J. Springer, Influence of the mesophase structure on the β-relaxation in comb-like polymethacrylates, *Macromolecules*, 1995, **28**, 6254–6257.
42 H. Vogel, Das Temperaturabhängigkeitsgesetz der Viskosität von Flüssigkeiten, *Phys. Z*, 1921, **22**, 645–646.
43 G. S. Fulcher, Analysis of Recent Measurements of the Viscosity of Glasses, *J. Am. Ceram. Soc.*, 1925, **8**, 339–355.
44 G. Tammann and W. Hesse, Die Abhängigkeit der Viskosität von der Temperatur bei unterkühlten Flüssigkeiten, *Z. Anorg. Allg. Chem.*, 1926, **156**, 245–257.
45 C. A. Angell, Entropy and Fragility in Supercooling Liquids, *J. Res. Natl. Inst. Stand. Technol.*, 1997, **102**, 171–185.
46 E. Donth, The Size of Cooperatively Rearranging Regions at the Glass Transition, *J. Non-Cryst. Solids*, 1982, **53**, 325–330.
47 M. Beiner and R. Huth, Nanophase separation and hindered glass transition in side-chain polymers, *Nat. Mater.*, 2003, **2**, 595–599.
48 A. Yildirim, C. Krause, P. Huber and A. Schönhals, Multiple glassy dynamics of a homologous series of triphenylene-based columnar liquid crystals – A study by broadband dielectric spectroscopy and advanced calorimetry, *J. Mol. Liq.*, 2022, **358**, 119212.
49 A. Yildirim, C. Krause, R. Zorn, W. Lohstroh, M. Zamponi, O. Holderer, B. Frick and A. Schönhals, Complex molecular dynamics of a symmetric model discotic liquid crystal revealed by broadband dielectric, thermal and neutron spectroscopy, *Soft Matter*, 2020, **16**, 2005–2016.
50 A. Yildirim, A. Bühlmeyer, S. Hayashi, J. C. Haenle, K. Sentker, C. Krause, P. Huber, S. Laschat and A. Schönhals, Multiple Glass Dynamics in Dipole Functionalized Triphenylene Based Discotic Crystals Revealed by Broadband Dielectric Spectroscopy and Advanced Calorimetry – Assessment of the Molecular Origin, *Phys. Chem. Chem. Phys.*, 2019, **21**, 18265–18277.
51 J. C. Dyre and T. B. Schroder, Universality of ac conduction in disordered solids, *Rev. Mod. Phys.*, 2000, **72**, 873–892.
52 A. K. Jonscher, The 'Universal' Dielectric Response, *Nature*, 1977, **267**, 673–679.
53 I. Popov, H. Zhu, A. Khamzin, C. Zanelotti, L. Madsen, M. Forsyth and A. P. Sokolov, Collective ion dynamics in ionicliquid crystals: The origin of conductivity suppression, *J. Chem. Phys. C*, 2023, **127**, 15918–15927.
54 C. Krause, R. Zorn, B. Frick and A. Schönhals, Thermal properties and vibrational density of states of a nanoconfined discotic liquid crystal, *Colloid Polym. Sci.*, 2014, **292**, 1949–1960.
55 M. Wübbenhorst and J. van Turnhout, Analysis of Complex Dielectric Spectra. I. One-Dimensional Derivative Techniques and Three-Dimensional Modelling, *J. Non-Cryst. Solids*, 2002, **305**, 40–49.
56 A. Serghei, M. Tress, J. R. Sangoro and F. Kremer, Electrode polarization and charge transport at solid interfaces, *Phys. Rev. B: Condens. Matter Mater. Phys.*, 2009, **80**, 184301.
57 Z. Song, C. Rodriguez-Tinoco, A. Mathew and S. Napolitano, Fast Equilibration Mechanisms in Disordered Materials Mediated by Slow Liquid Dynamics, *Sci. Adv.*, 2022, **8**, 1–7.
58 R. P. White, S. Napolitano and J. E. G. Lipson, Mechanistic picture for the slow Arrhenius process in glass forming liquids systems: The Collective small displacement model, *Phys. Rev. Lett.*, 2025, **134**, 098203.
59 F. Caporaletti, H. Bock and S. Napolitano, Slow liquid dynamics promotes ordering in a columnar liquid crystalline glass-former, *J. Mol. Liq.*, 2025, **433**, 127902.
60 K. Sentker, A. W. Zantop, M. Lippmann, T. Hofmann, O. H. Seeck, A. V. Kityk, A. Yildirim, A. Schönhals, M. G. Mazza and P. Huber, Quantized Self-Assembly of Discotic Rings in a Liquid Crystal Confined in Nanopores, *Phys. Rev. Lett.*, 2018, **120**, 067801.
61 K. Sentker, A. Yildirim, M. Lippmann, A. W. Zantop, F. Bertram, T. Hofmann, O. H. Seeck, A. V. Kityk, M. G. Mazza, A. Schönhals and P. Huber, Self-assembly of liquid crystals in nanoporous solids for adaptive photonic metamaterials, *Nanoscale*, 2019, **11**, 23304–23317.
62 A. V. Kityk, M. Busch, D. Rau, S. Calus, C. V. Cerclier, R. Lefort, D. Morineau, E. Grelet, C. Krause, A. Schönhals, B. Frick and P. Huber, Thermotropic orientational order of discotic liquid crystals in nanochannels: an optical polarimetry study and a Landau de Gennes analysis, *Soft Matter*, 2014, **10**, 4522–4534.
63 R. Zhang, X. Zeng, M. Prehm, F. Liu, S. Grimm, M. Geuss, M. Steinhart, C. Tschierske and G. Ungar, Honeycombs in Honeycombs: Complex Liquid Crystal Alumina Composite Mesostructures, *ACS Nano*, 2014, **8**, 4500–4509.
64 A. Yildirim, K. Sentker, G. J. Smales, B. R. Pauw, P. Huber and A. Schönhals, Collective orientational order and phase behavior of a discotic liquid crystal under nanoscale confinement, *Nanoscale Adv.*, 2019, **1**, 1104–1116.

